

Time evolution of filamentation and self-generated fields in the coronae of directly driven inertial-confinement fusion capsules

F. H. Séguin,¹ C. K. Li,¹ M. J.-E. Manuel,¹ H. G. Rinderknecht,¹ N. Sinenian,¹ J. A. Frenje,¹ J. R. Rygg,^{1,a)} D. G. Hicks,^{1,a)} R. D. Petrasso,¹ J. Delettrez,² R. Betti,^{2,b),c)} F. J. Marshall,² and V. A. Smalyuk^{2,a)}

¹Plasma Science and Fusion Center, Massachusetts Institute of Technology, Cambridge, Massachusetts 02139, USA

²Laboratory for Laser Energetics, University of Rochester, Rochester, New York 14623, USA

(Received 20 April 2011; accepted 27 October 2011; published online 9 January 2012)

Time-gated radiography with monoenergetic 15-MeV protons, 3-MeV protons, and 4-MeV alpha particles has revealed a rich and complex evolution of electromagnetic field structures in and around imploding, directly driven inertial-confinement fusion (ICF) targets at the OMEGA laser facility. Plastic-shell capsules and solid plastic spheres were imaged during and after irradiation with ICF-relevant laser drive (up to 6×10^{14} W/cm²). Radial filaments appeared while the laser was on; they filled, and were frozen into, the out-flowing corona, persisting until well after the end of the laser drive. Data from specially designed experiments indicate that the filaments were not generated by two-plasmon-decay instabilities or by Rayleigh-Taylor instabilities associated with shell acceleration. Before the onset of visible filamentation, quasi-spherical field structures appeared outside the capsule in the images in a form that suggests outgoing shells of net positive charge. We conjecture that these discrete shells are related to multiple peaks seen previously in the spectra of protons ablated from the targets. © 2012 American Institute of Physics. [doi:10.1063/1.3671908]

I. INTRODUCTION

In direct-drive inertial-confinement fusion (ICF), a fuel capsule must be compressed through laser illumination in order to bring the fuel to the high temperature and density necessary for fusion and ignition.¹ This process requires the transfer of energy from the laser light to the capsule, but the laser light cannot penetrate the critical-density surface that is outside the capsule; this means that thermal energy deposited near the critical surface must be transported across a small gap in order to reach the capsule. It has been noted that the existence of any strong electric (E) or magnetic (B) fields in this region during laser drive could compromise the energy transport,² but investigation of possible fields in ICF-relevant experiments have been limited.

Experiments in non-ICF contexts have provided radiographic evidence of filaments formed in the interactions of lasers with plastic and glass,^{3–9} and these filaments have been attributed to electrothermal instabilities.¹⁰ ICF experiments have revealed several types of self-generated fields in and around laser-illuminated capsules. These include an external, radial E field due to net charging of laser-illuminated capsules to potentials of order 0.5 MV (indicated by an upshift in the energy of charged fusion products as they leave the capsule^{11,12}), and also external, nonradial E or B fields¹³ that generated angular variations in the fluence of charged fusion products by changing their trajectories without changing their energies. Recent experiments utilizing

monoenergetic-proton radiography¹⁴ provided evidence of radial fields inside direct-drive capsules¹⁵ and filamentary structure in the corona of a fast-ignition type, cone-in-shell target.¹⁶ Ref. 16 showed a radiographic image recorded well after the laser drive was off, and it was not determined whether the filamentary structure was present during the laser pulse when it could have an impact on implosion performance. Another experiment utilizing quasi-monoenergetic protons to make radiographs revealed no filaments around a directly driven capsule,¹⁷ though the laser drive intensity was an order of magnitude lower than that considered here.

In this article we expand greatly on earlier observations to show when the filamentary structures appear, how they evolve in time, and how they differ for a few different target types and laser illumination intensities. In particular, we show that filamentation does appear during laser drive and may therefore affect the laser drive. Section II describes the experiments. Different laser intensities were used to look for evidence of whether filamentation is connected with the two-plasmon-decay (TPD) instability,¹⁸ and both hollow fuel capsules and solid plastic spheres were used to look for evidence of any direct causal connection between implosion-related Rayleigh-Taylor (RT) instabilities¹ and filamentation. Section III presents an overview of the images, and in Sec. IV the characteristics of the filamentation in the images is discussed, along with some aspects of image formation. In Sec. V, radiographs of imploding capsules recorded before the formation of filaments are discussed; they appear to provide information about radial electric fields that may bear on interesting features in the spectra of protons ablated from direct-drive targets.^{19,20} Section VI is about effects of

^{a)}Present address: Lawrence Livermore National Laboratory, Livermore, California.

^{b)}Also at Department of Physics and Astronomy, University of Rochester.

^{c)}Also at Department of Mechanical Engineering, University of Rochester.

different drive intensities, Sec. VII briefly considers the difference between images of direct- and indirect-drive implosions, and Secs. VIII and IX contain final discussion. Several details are discussed in appendices.

II. EXPERIMENTS

Three types of monoenergetic charged particles were used to radiograph $\sim 850\text{-}\mu\text{m}$ -diameter CH targets driven by 40 OMEGA laser beams,²¹ as shown in Fig. 1. Targets included solid CH spheres as well as capsules with 20- μm - and 35- μm -thick CH shells with H_2 fill. The solid spheres were used to eliminate radial acceleration and thus eliminate any shell-acceleration-related RT instability as a possible source of filamentation. To test the possibility that the filaments were generated by the TPD instability, which has a threshold of $\sim 5 \times 10^{14} \text{ W/cm}^2$,²² several different on-target laser intensities were used; these included 2×10^{14} and $6 \times 10^{14} \text{ W/cm}^2$ in square pulses, and 1×10^{14} and $4 \times 10^{14} \text{ W/cm}^2$ within a shaped pulse.

The backlighting source of charged particles was a thin glass shell with D^3He fill, driven by 20 OMEGA beams and producing D^3He protons, DD protons, and D^3He alphas, all upshifted slightly in energy to ~ 15.0 , 3.3, and 4 MeV, respectively (Fig. 1(c)), due to capsule charging.^{11,12} Separate radiographic images resulting from the fluences of each of these three particles (e.g., Fig. 1(b)) were recorded by a detector pack, which registers the position and energy of

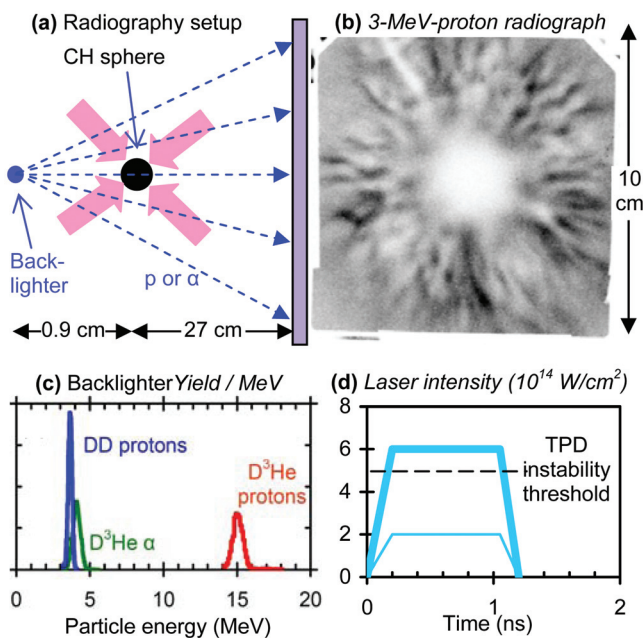


FIG. 1. (Color) Experimental setup (a), sample radiograph (b), backlighter spectrum (c), and time history of two laser drive options (d) used on solid CH spheres. In (a), the dashed blue lines represent trajectories of charged particles from the backlighter, and the violet rectangle is the detector (which, with a $10 \text{ cm} \times 10 \text{ cm}$ surface, records an area $3 \text{ mm} \times 3 \text{ mm}$ at the subject. Darkness in the image (b) is proportional to proton fluence). The backlighter-subject and subject-detector distances shown in part (a), used for the radiographs in Figs. 2 and 4, give an imaging magnification of 31. Since 10 cm is the size of the detector, the field of view at the subject is about 3 mm. The images in Fig. 3 have similar, but slightly different, magnifications. Image (b) is from OMEGA shot 51237.

each individual particle²³ on two layers of CR-39 nuclear track detector. For each particle type, it is possible to make two images: fluence vs. position and mean particle energy vs. position.

Relative timing of the lasers driving the backlighters and the CH subject spheres was adjusted so that particles produced during the $\sim 120\text{-ps}$ backlighter burn would be incident on the subject at any desired time during or after the subject drive. The timing was verified during experiments by using the proton temporal diagnostic.²⁴

Fluence images recorded with 15-MeV protons at different times relative to the subject drive laser are shown in Figs. 2–4 (see also Appendix B). Figure 5 shows how sample fluence images relate to their corresponding energy images. The images show the target structure as well as external fields, including fields associated with coronal filamentation that generate radial striations in the images by deflecting the backlighter-generated charged particles.

Spatial resolution of the imaging system is largely a function of the size of the source, which has typically been measured^{25,26} to be approximately Gaussian with FWHM $\sim 45 \mu\text{m}$. This is not much smaller than the apparent width of the narrowest image striations seen in Figs. 2 through 4, so an important question is whether it obscures smaller features that might be important to the overall filament structure or whether it even combines multiple striations into single ones. To determine this, we imaged a related laser-plasma interaction simultaneously with the backlighter and detector described here and with a backlighter formed by a 10- μm -diameter, 10-ps-long beam from OMEGA EP (Ref. 27) striking an Au foil. As shown in Appendix A, the same number and size of image striations are seen in both images, although the edges are more sharply defined in the images from the higher-resolution EP-driven backlighter. Therefore, the images shown here have not lost essential structural information relative to that obtainable with the higher-resolution EP-based method. More work is now being planned for the EP-based system, as described in Ref. 28 (which also includes preliminary late-time images of implosions indicating the same basic number and widths of filaments seen here).

III. OVERVIEW OF THE IMAGES

Each image shows a circular target at the center. In the case of the solid spheres (Fig. 2), this is a region of low proton fluence on the detector (white), which is the shadow of the CH sphere (the protons lost enough energy to not appear in the selected energy window of $\sim 13.5\text{--}15.5 \text{ MeV}$). In the case of the hollow capsules (Figs. 3 and 4), a low-fluence circle is seen at the location of the capsule shells (see the left images of Figs. 3 and 4) until $\sim 2 \text{ ns}$, when the capsule reaches nearly maximum compression (see the latest-time images in Figs. 3 and 4 as well as part (c) of Fig. 5). More discussion about what radiographs indicate about the dynamics of the capsule itself and its internal structure can be found in Ref. 15.

In Figs. 2 through 4, all fluence images show signs of electromagnetic fields in the corona after the laser drive has been on for a length of time that depends on the laser

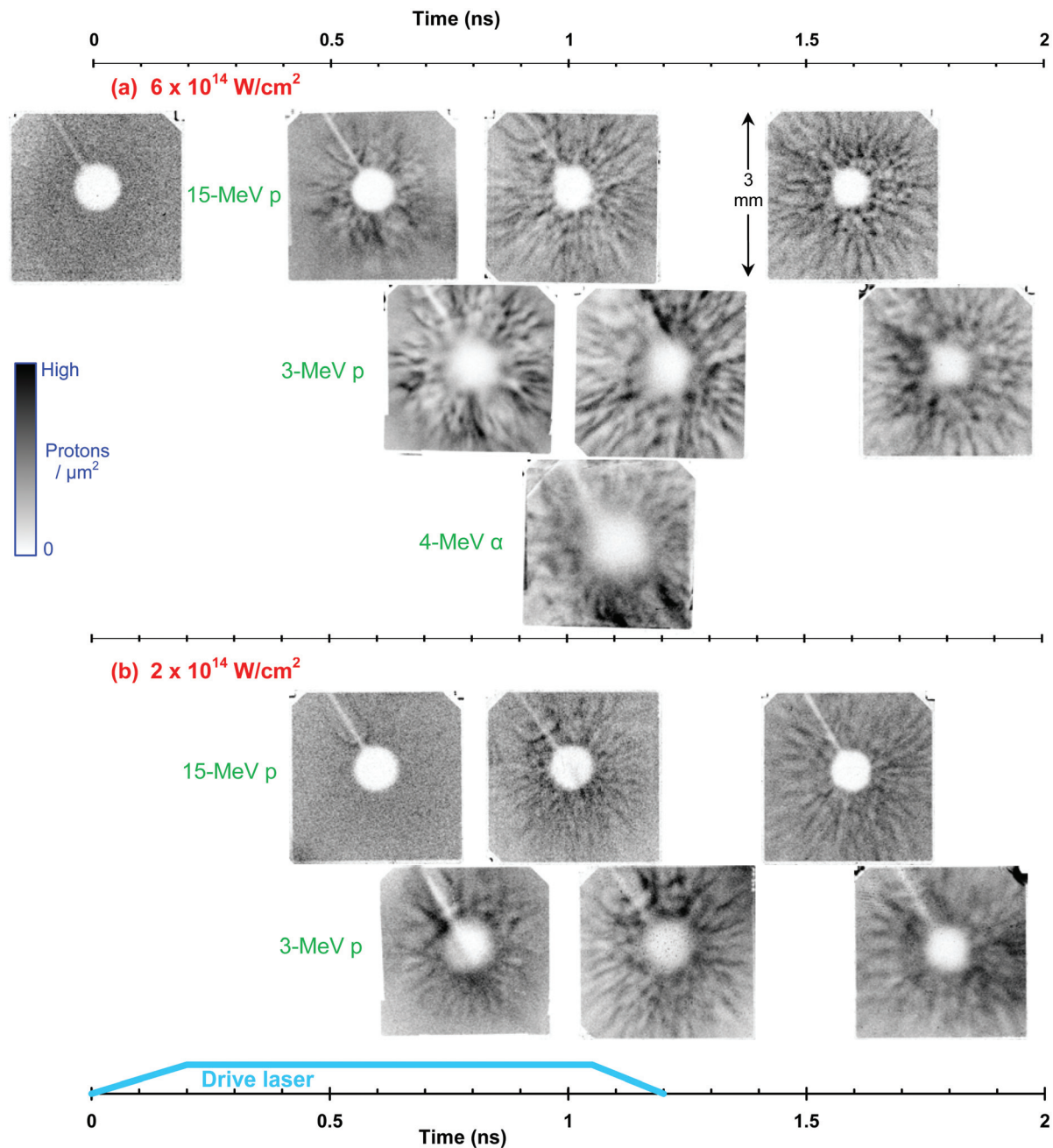


FIG. 2. (Color) Monoenergetic charged-particle fluence radiographs of solid CH spheres recorded at different times relative to the laser drive for two drive intensities (6×10^{14} and 2×10^{14} W/cm²) and three particle types (15-MeV p, 3-MeV p, and 4-MeV α). The white diagonal line in each upper left corner is the stalk holding the subject. The size of the field of view at the subject is about 3 mm. The maximum fluence is different for each image, but is generally ~ 1 proton per μm^2 at the subject. The OMEGA implosions on which the 15-MeV images were recorded were, from left to right, 51243, 51237, 51238, and 51239 in (a); 51240, 51241, and 51242 in (b).

intensity. In some cases (Fig. 3), the first structure to appear outside the target is quasi-spherical. Figure 5(b) shows that this feature is related to fields, rather than matter, because it does not cause any energy loss in the backlighting particles forming the image. These features will be discussed in Sec. V. As time progresses in Fig. 3, the quasi-spherical structure seems to break up until, by 0.65 ns, a transition to a structure more like radial image striations due to filamentation occurs. The quasi-spherical structure does not appear in every image sequence, but all of the targets developed filamentation during the laser drive. Like the quasi-spherical structures, these striations do not appear in the energy images (Figs. 5(a) and

5(c)), so they also appear to be caused by fields. This is discussed in Sec. IV. Many fluence images, especially in Fig. 3, show features around the stalks (upper left corner) that have no counterpart in the corresponding energy images (Fig. 5). These features indicate fields, which are under study and will be discussed elsewhere.

IV. FILAMENTATION

A. Some characteristics of the filaments

Figures 2 and 3 show that filamentation appears during the laser drive and persists long after the drive is off. When

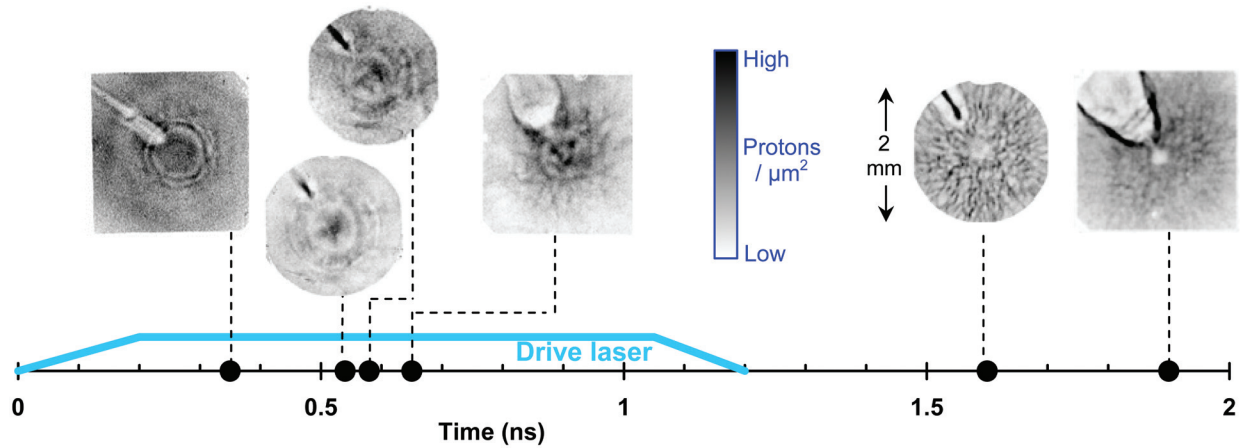


FIG. 3. (Color) 15-MeV-proton fluence radiographs of 860- μm -diameter capsules with 20- μm -thick CH shells and 15-atm H_2 fill, recorded at different times relative to the laser drive ($6 \times 10^{14} \text{ W/cm}^2$). See Ref. 15 for a radiographic study of fields inside the capsules in these kinds of implosions. From left to right, the images are from OMEGA shots 49119, 46536, 46537, 49120, 46535, and 49122.

they first appear, filaments are confined to a region within an expanding sphere. More information about this region can be seen in Fig. 6, which shows three fluence images from a single OMEGA implosion. Each represents a different imaging particle and thus a different sampling time (due to the different flight times of the particles from backlighter to subject). The positions of the outer ends of the filaments coincide fairly well with the outer boundary of the corona as predicted by 1-D simulations.²⁹ In both data and simulations, this outer boundary moves outward at an apparent radial velocity of $\sim 2000 \mu\text{m/ns}$. That velocity exceeds the ion acoustic velocity by a factor of 5–10, which is in rough agreement with predictions of a complete model of the free-streaming expansion of ions into vacuum, including charge-separation effects.³⁰

While the data indicate that filaments extend radially to the outer boundary of the corona (at least for times < 1 ns when the outer boundary is within the radiographic field of view), the important question of whether the inner ends of the filaments terminate in the under-dense plasma or extend inside the critical density surface is more difficult and will be touched upon in Sec. IV C.

The individual filaments are roughly radial, but they have ripples and occasional bifurcations; some of these specific features can be identified in two or three of the images of Fig. 6, indicating that individual filaments and even their detailed structures are frozen into the outgoing coronal plasma for at least a few hundred ps. (Successive images at a given backlighter energy cannot be compared in this way, since each image group (15-MeV protons, 3-MeV protons, and sometimes 4-MeV alpha particles) is from a separate implosion.)

As mentioned in Sec. III, the image striations cannot be due to coronal filaments of matter because the detected backlighter particles' energies show no signs of having been reduced. In addition, the images contain both light striations (indicating a proton fluence deficit relative to the average) and dark striations (indicating a fluence excess), whereas a filament of mass without fields will diminish backlighter-particle energy and will generate a light striation by some combination of ranging the particle energy down to below the limit of the detector and scattering the particles. The protons forming the images must therefore have had their trajectories bent by E or B fields that focused or defocused them without affecting their energies. This means that the width of an

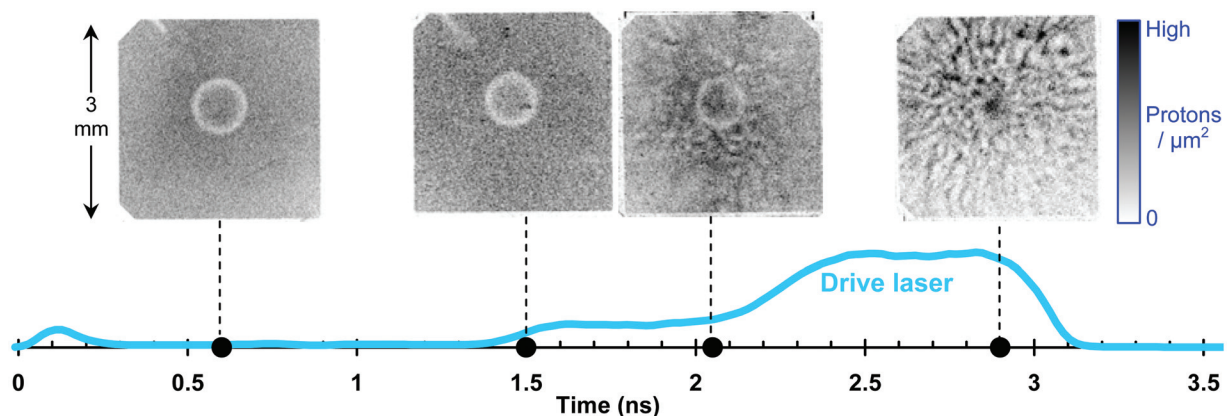


FIG. 4. (Color) 15-MeV-proton fluence radiographs of 850- μm -diameter capsules with 35- μm -thick CH shells and 15-atm H_2 fill. The capsules were driven with 40 laser beams in a shaped pulse (OMEGA type RD1501p). The drive has an initial picket, followed after about 1.3 ns by a plateau with intensity $\sim 1 \times 10^{14} \text{ W/cm}^2$ (~ 1.5 – 2.1 ns) and another with intensity $\sim 4 \times 10^{14} \text{ W/cm}^2$ (~ 2.4 – 2.9 ns). From left to right, the images are from OMEGA shots 51244, 51246, 51247, and 51250.

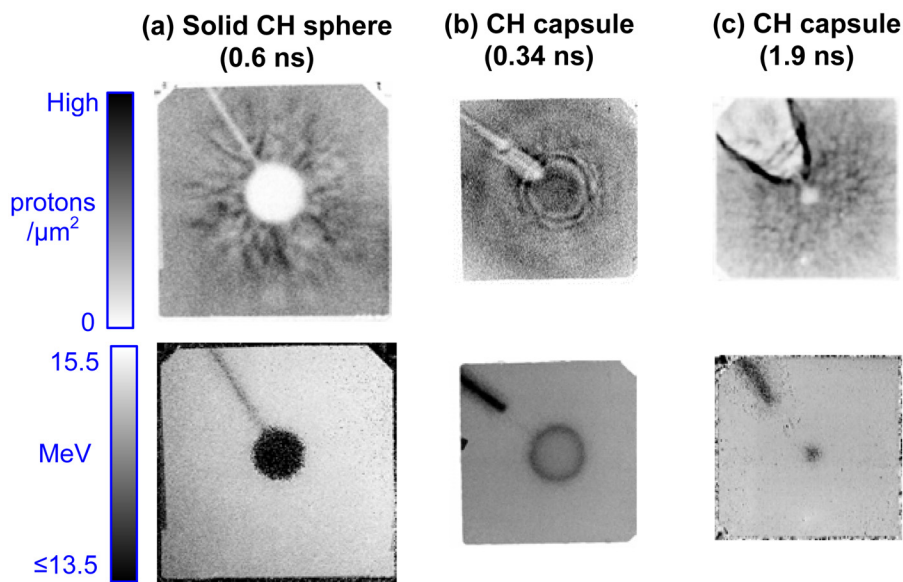


FIG. 5. (Color online) Pairs of proton-fluence and proton-mean-energy images. In each case, the CH target and the stalk in the upper left leave their signatures in the energy image, while the radial filaments (parts (a) and (c)) and other field-related structures do not. The fluence images are from (a) Fig. 2(a), (b) Fig. 3, and (c) Fig. 3. See also Fig. 13 for more information about part (b).

image striation reflects not the physical width of a filament or even the physical extent of the fields, but a combination of the strength and physical extent of the fields. Figures 7 and 8 show the basic experiment geometry and illustrate two kinds of filaments that could generate image striations.

Qualitatively, the light striations appear to dominate, particularly in the high-laser-intensity cases and the images made with lower-energy particles where striations are widest. In the 3-MeV-p image of Fig. 6 both light and dark striations can be seen, but the dark striations appear to the observer to be behind, and partially obscured by, the light striations. Sometimes the dark striations shadow the light ones on one or both sides, appearing to be either correlated or part of the same structure, but sometimes light and dark structures appear alone.

B. Formation of image striations by fields around filaments

A filament with a perpendicular E field (Fig. 7(a)) would create an image striation either light (Fig. 7(b)) or dark

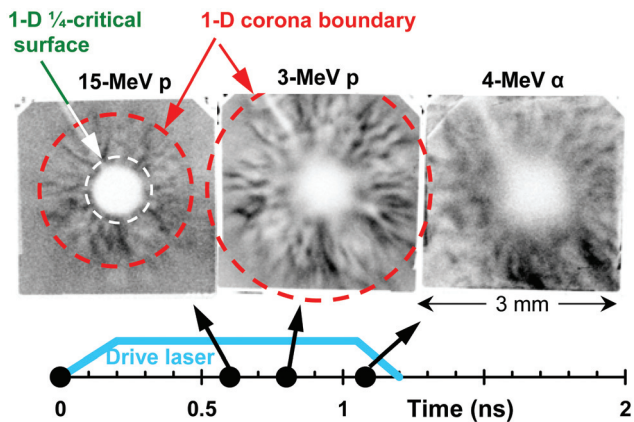


FIG. 6. (Color) Radiographs made with three different monoenergetic particles during OMEGA implosion 51237, compared with radii for the $1/4$ -critical surface and the outer corona boundary predicted by the 1-D simulation code LLAC.²⁹ This implosion utilized a laser intensity of 6×10^{14} W/cm².

(Fig. 7(c)), depending on the sign of E . Such a field could be caused by plasma pressure gradients, but we will use a simple model in which it is due to a net line charge λ on the filament. The angular deflection $\Theta_{i,E}$ of a charged particle of type i would be

$$\Theta_{i,E} = \frac{q_i}{2\epsilon_i} \left| \int E \times dl \right| \propto \frac{q_i}{\epsilon_i} \frac{1}{\sin \phi} \lambda, \quad (1)$$

where the integral is taken over the trajectory of a particle with charge q_i and energy ϵ_i , and ϕ is the angle between a specific filament and a specific particle trajectory as shown in Fig. 7(a).

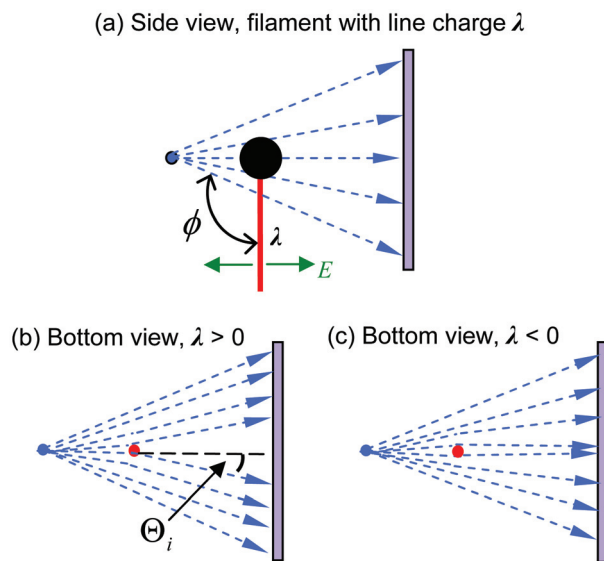


FIG. 7. (Color) Illustrations showing how E fields (green) around a line charge (red) can deflect trajectories of positively charged ions (blue dashed lines) passing from the particle source to the detector plane (violet). (a) Side view of system. (b) Bottom view when $\lambda > 0$, resulting in a fluence-deficit (light) image striation. (c) Bottom view when $\lambda < 0$, resulting in a fluence-excess (dark) image striation. As described in the text, ϕ is the angle between a specific filament and a specific particle trajectory, while Θ_i is the particle deflection angle.

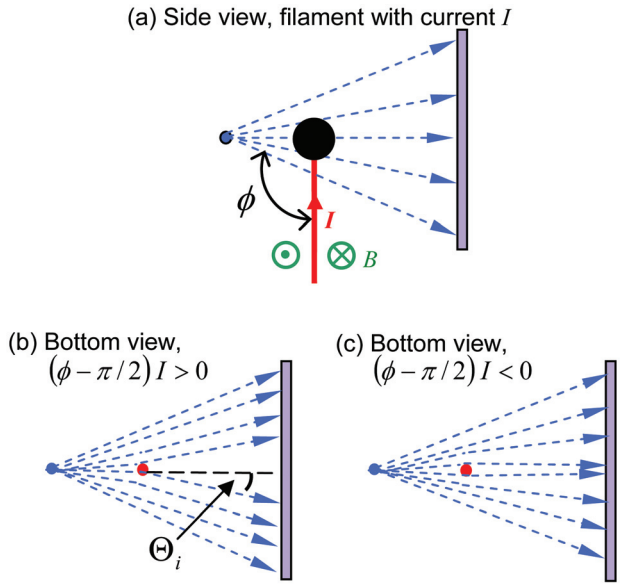


FIG. 8. (Color) Illustrations showing how B fields (green) around a line current (red) can deflect trajectories of positively charged ions (blue dashed lines) passing from the particle source to the detector plane (violet). (a) Side view of system. (b) Bottom view when $(\phi - \pi/2)I > 0$, resulting in a light (fluency-deficit) image striation. (c) Bottom view when $(\phi - \pi/2)I < 0$, resulting in a dark (fluency-excess) image striation.

A filament surrounded by a toroidal magnetic field B can also generate either a light or dark image striation, as shown in Fig. 8(a), depending on the sign of B and also depending on whether the angle ϕ is larger or smaller than $\pi/2$ (there is minimal deflection if $\phi \approx \pi/2$). The field could be generated by noncollinear temperature and density gradients or by a linear current I . In the later case

$$\Theta_{i,B} = \frac{q_i}{\sqrt{2m_i\varepsilon_i}} \left| \int B \times d\ell \right| \propto \frac{q_i}{\sqrt{m_i\varepsilon_i}} \frac{\cos \phi}{\sin \phi} I, \quad (2)$$

where m_i is the particle mass.

Simulations show that if a current or charge filament has a surrounding field that extends a long distance away, the resultant image striation will generally have only a fluency-deficit or fluency-excess structure no matter what the field strength or imaging geometry is. This is because the deflection angle of a particle traveling through a field that decreases as the inverse of the distance from the filament is independent of the particle's impact parameter for moderate scattering angles. Either field type can result in an image striation with either a fluency deficit or a fluency excess, depending on the field sign. Increasing the lateral radius of the current- or charge-containing region decreases the field strength near the center and results in a diminished amplitude of the fluency deficit or excess in an image striation. The lateral field radius will in practice probably be limited due to charge screening, diffuse return currents, or other processes. Simulations show that if the field extends only a short distance from the filament, and if the field is strong enough, then it can produce an image striation with parallel fluency-deficit and fluency-excess components. In the cases represented by Figs. 7(b) and 8(b), the result is a fluency-excess shoulder on the sides of a deficit region. In the cases repre-

sented by Figs. 7(c) and 8(c), the result of a very strong field and very small lateral field extent can be that the deflected protons cross over each other and leave a central deficit surrounded by fluency-excess areas as shown in Fig. 9 (without the limit on field extent, particles deflected at larger impact parameters fill in the deficit).

C. Information in the images about field type

The question of whether the filament-related fields generating the image striations are dominated by E or B is important, since a B field is probably more dangerous for transport of energy from the critical surface to the ablation surface. Any given image striation structure that can be modeled with B fields around a current filament can be duplicated with an appropriate E field, and vice versa, so the morphology of individual striations does not help. The two things that are different for the two kinds of fields (Eqs. (1) and (2)) are the dependences of the deflection angle Θ on backlighter-particle energy ε and on the angle ϕ between the particle trajectory and a specific filament.

If the fields around the filaments extended hundreds of microns from the filaments, then individual striations would be either all fluency or all deficit and would have widths of striations proportional to the angles shown in Eqs. (1) and (2). Theoretically, the measured ratio of widths in images from two different backlighter-particle energies would then determine the field type since $\Theta \propto \varepsilon^{-1}$ for electric fields and $\Theta \propto \varepsilon^{-1/2}$ for magnetic fields. However, this relationship breaks down if the field is restricted to a region within a small lateral radius from the filament. The actual width depends on a combination of current or charge density, the field outer radius and, to some extent, on the lateral radius of the charge-carrying or current-carrying part of the filament.

On the other hand, even though the morphology of any individual striation can be modeled equally well with either E fields or B fields, the difference in dependence on ϕ changes the overall balance of striations in the image. For E fields, it means (Eq. (1)) that there is some variation in striation contrast for filaments at different ϕ , but for B fields, it means (Eq. (2)) there is huge variation: current filaments roughly parallel to the image plane produce almost no image striations. The difference is illustrated in Fig. 10, which shows simple Monte Carlo simulations of images that could result for the two cases if all filaments had the same length. In the simulations formed assuming B fields, the ϕ dependence causes the outer boundary of the region with striations to be

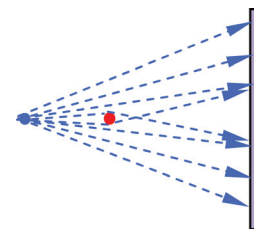


FIG. 9. (Color) Cartoon showing how the scenario of either Fig. 7(c) or 8(c) might result in a fluency deficit surrounded by fluency excess regions, but only if a strong deflecting field is restricted to a small region around the filament.

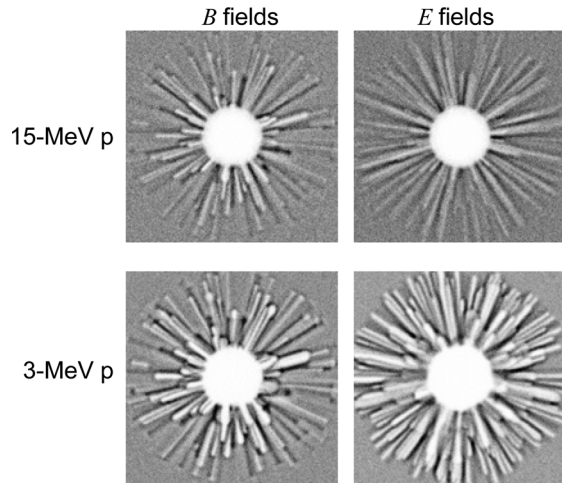


FIG. 10. Simple Monte Carlo simulations of images formed when a solid, 880- μm -diameter CH sphere is assumed to be surrounded by 200 filaments that are randomly placed in angle and extend from the CH surface to an outer radius of 1600 μm (all simulations use the same filament angles). The imaging geometry was as shown in Fig. 1, and backlighting protons were assumed to come from a 10-keV D^3He plasma with a FWHM of 45 μm . The fields were truncated at a lateral distance of 100 μm from each filament and were simply set to zero beyond the end.

vaguely defined. The images made assuming E fields are somewhat different, with a harder outer striation boundary.

Although the parameters have not been completely optimized for the purpose, and are not claimed to be unique, the outer filament boundary looks a little more like that of Fig. 1(b) in the E -field simulations than it does in the B -field simulations. On the other hand, the E -field simulations lack isolated fluence-excess features in the 15-MeV image, as seen in the 0.6-ns image of Fig. 2(a). The B -field simulations benefit from having dark striations for all filaments that are closest to the backlighter if all currents point toward the target, while the same effect is harder to achieve with E fields (see Fig. 11(b)). The B -field alternative is also suggested by the observation that the filament structure appears “frozen in,” as discussed in Sec. IV A.

Further work with analytic calculations and Monte Carlo simulations, exploring a wider range of parameters, is under way in an effort to arrive at a more definitive conclusion about field type.

D. Filament time evolution and spatial distribution

From the images of Fig. 2, it can be seen that filamentation definitely developed during the 1-ns laser drive of the solid spheres. It appeared for both laser intensities used, but with the higher intensity it appeared slightly earlier and resulted in slightly larger field amplitudes. Not enough images were recorded to provide a complete picture of the growth phase, but it is clear that the amplitude grew from nearly zero to nearly its peak value within the time interval between 0.6 ns and 0.8 ns for the $2 \times W/\text{cm}^2$ case. It persisted until the last measurements at 1.8 ns, long after the laser drive was off.

We note that even at 1.8 ns, when the laser had been off for almost 1 ns, the inner ends of the filaments still appear in Figs. 2 to come close to the surface of the CH sphere. In the

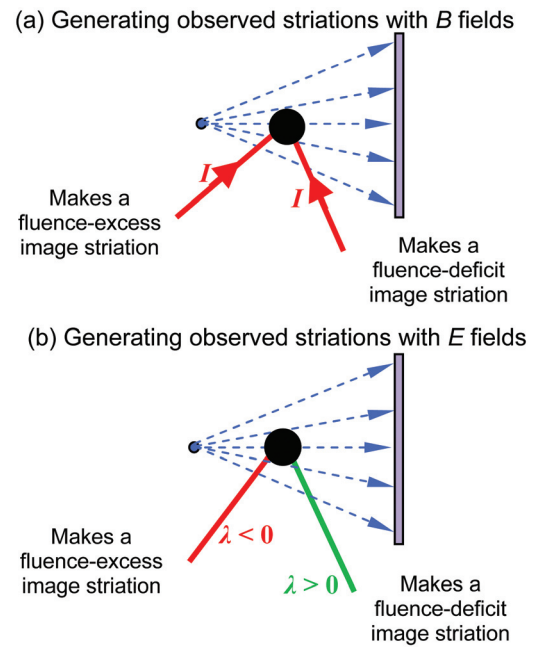


FIG. 11. (Color) Cartoons showing why it may be easier to explain one aspect of image striations with B fields than with E fields, using the observation that fluence-deficit striations appear to be formed by filaments that are closer to the detector plane than those associated with fluence-excess filaments. Current filaments can generate this characteristic if they all have the same current direction (a), while line-charge filaments can do so only in an unphysical arrangement in which filaments closer to the detector have one charge sign while filaments farther than the detector have the other (b).

left image of Fig. 6, some of the inner ends appear to penetrate inside the $1/4$ -critical surface and possibly touch the ablation surface. However, it is not currently possible to arrive at a definitive conclusion as to whether this is true; since most of the striations in the images correspond to filaments that tilt either toward or away from the detector (i.e., ϕ greater or smaller than $\pi/2$ in Fig. 7(a) or 8(a)), their projections in the detector plane could appear to touch the ablation surface even if their inner ends terminated well outside the critical surface, as shown in Fig. 12. This leaves ambiguity as to whether thermal transport from the critical surface to the ablation surface could be affected by fields there.

The spatial distribution of the filaments, and the ripples and bifurcations, give the appearance of a certain amount of randomness. However, there is some regularity in the angular intervals between filaments that suggests an underlying mode structure in the angular distribution.

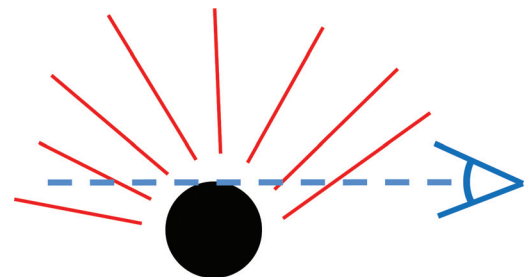


FIG. 12. (Color) Diagram illustrating how lines of sight of an observer could make radial filaments appear to intersect the projection of the surface of a sphere even if they did not actually touch it.

The number of filaments is not easy to extract directly from the images, which are 2-dimensional projections of a 3-dimensional structure. However, the synthetic images shown in Fig. 10 were compared with others utilizing different numbers of current or charge filaments distributed around the target surface, and it was found that roughly 200 filaments (within a factor of 2) were required to match the density of striations in the actual images of CH spheres for drive intensity 6×10^{14} W/cm²; this corresponds to a linear spacing between filaments of about 100 μm near the ablation surface, which is at a radius of ~ 375 μm at 1 ns according to 1-D LILAC simulations.

The effective filament linear charge density required to explain the striations (if E fields are involved) depends on the lateral size of the field region, but to get reasonable simulations it is necessary to use the equivalent of $\sim 2 \times 10^6$ protons/ μm . If the fields are predominantly due to currents, a minimum of ~ 2 kA per filament is required. This would generate $|B| \sim 10$ T at a lateral distance from the filament center of 40 μm . For plasma conditions near the ablation surface, such a field would result in a Hall parameter of ~ 1 , which could be problematic for thermal energy transport.

V. EXTERNAL FIELDS WITH SPHERICAL SYMMETRY BEFORE FILAMENTATION

The three images in Fig. 3 that were recorded after the onset of laser drive and before filamentation (at 0.35, 0.54, and 0.58 ns) show quasi-spherical features in the form of radial oscillations in fluence outside the target, as shown in Fig. 13. Monte Carlo simulations in Fig. 14 show that this structure is consistent with shells of net positive charge (equivalent to $\sim 1 \times 10^{11}$ protons, in the case of the first charge shell outside the CH capsule shell).

If the charge shells consist of discrete bunches of protons travelling outward, they could be related to an interest-

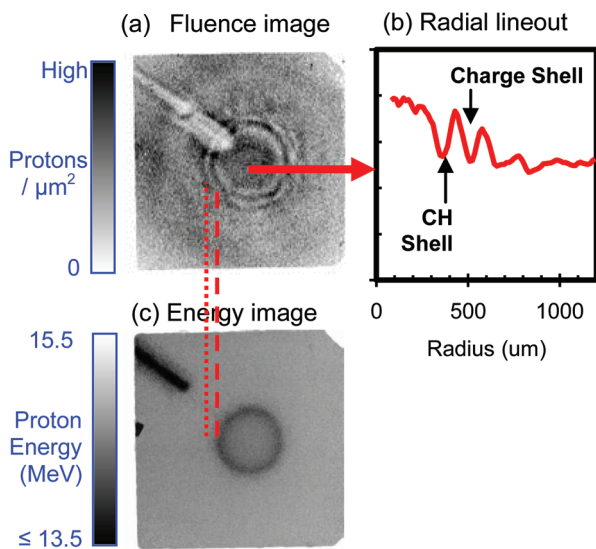


FIG. 13. (Color) Radial lineout (b) of fluence image (a) from Fig. 3, and the corresponding mean-proton-energy image (c). Note that only the innermost circle of fluence deficit in (a), from the CH shell, has a counterpart in (c), so the radial oscillations outside the capsule shell seem to be due to radial electric fields.

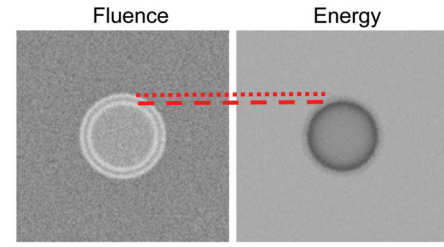


FIG. 14. (Color) Monte Carlo simulations illustrating how the images in Fig. 13 have the signature of a CH shell plus charge shells. In this case, a charge shell with 5×10^{10} protons was placed outside a hollow CH capsule.

ing structure seen in many spectra of ablator protons, as shown in Fig. 15 and described in Ref. 19 as potentially representing ion acoustic perturbations in an expanding plasma. The spectrum shown in Fig. 14, recorded during an implosion of a CH-shell capsule driven by a 1-ns square OMEGA pulse with the higher drive intensity of $\sim 9 \times 10^{14}$ W/cm², has a series of peaks separated in energy in a well-defined manner. Such a series of peaks with different energies could result if a succession of discrete shells of positive charge were released sequentially. Each shell would remove some charge from the capsule, so that the next shell would experience less radial acceleration and thus have lower energy when it reaches the detector. It has also been suggested³¹ that this phenomenon could be connected to oscillations in the circuit formed by target, target-holding mechanism, and target chamber.

Although the laser drive intensity during the experiment generating the spectrum in Fig. 15 was 50% higher than that used in the implosions illustrated in Figs. 4 and 13, making a direct comparison less than ideal, a numerical comparison does indicate a possible connection. Each peak in the spectrum of Fig. 15 contains $\sim 2 \times 10^{12}$ protons. Other spectra measured in the same way (see Refs. 19 and 20) show considerable shot-to-shot variability in both the amplitude and the energy separation of the peaks, with some containing no peaks at all. A significant number of these spectra have peaks containing numbers of protons in the range $\sim 5 \times 10^{11}$ to

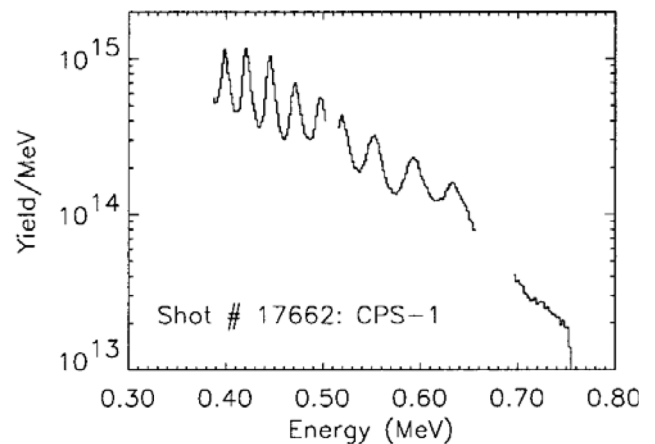


FIG. 15. A spectrum of accelerated ablator protons from an experiment at OMEGA, as presented and discussed in Ref. 19. This spectrum was recorded during an implosion with drive intensity 9×10^{14} W/cm², 50% higher than that used in Fig. 13.

5×10^{12} protons. Thus, the inferred number of $\sim 1 \times 10^{11}$ protons mentioned above in connection with Fig. 13 is not far away from what has been measured directly in experiments with somewhat higher laser intensities and makes future experiments involving simultaneous radiography and ablator-ion spectrometry attractive.

VI. EFFECTS OF DIFFERENT DRIVE INTENSITIES

The use of two different square pulses with drive intensities of 2×10^{14} W/cm² and 6×10^{14} W/cm², respectively, and a shaped pulse with plateaus at approximately 1×10^{14} W/cm² and 4×10^{14} W/cm², has allowed us to explore a narrow but significant range of drive conditions. The first conclusion is that filamentation may develop slightly earlier at higher intensities, as seen in the carefully controlled experiments with solid spheres and shown in Figs. 2 and 10, but that it occurs throughout this intensity range (and even at 1×10^{14} W/cm², as seen at the end of the low-intensity plateau in Fig. 4). Since 1×10^{14} W/cm² is substantially below the threshold of $\sim 5 \times 10^{14}$ for the TPD instability,²² this implies that the TPD instability is not the cause of filamentation.

The next, tentative, conclusion is that the occurrence of charge shells described in the previous section may have a substantial intensity dependence. They appear in three early time images for the drive intensity 6×10^{14} in two different experimental campaigns (Fig. 3 at 0.35, 0.53, and 0.58 ns), while they do not appear in the one pre-filament image for intensity 2×10^{14} (Fig. 2 at 0.6 ns). There is also no charge-shell structure visible in the pre-filament images of Fig. 4, but they were recorded after a very small amount of laser energy was delivered to the target at very low intensity ($\leq 0.5 \times 10^{14}$ W/cm²).

VII. COMPARISON TO INDIRECT-DRIVE IMPLOSIONS

All direct-drive ICF experiments we have radiographed so far have shown evidence of the type of coronal filament structure discussed here. In contrast, recent radiography data from indirect-drive ICF experiments^{32,33} have shown evidence of a very different kind of field structure (Fig. 16). Rather than filamentation with somewhat random structure, the radiographs show that between the fuel capsule and the

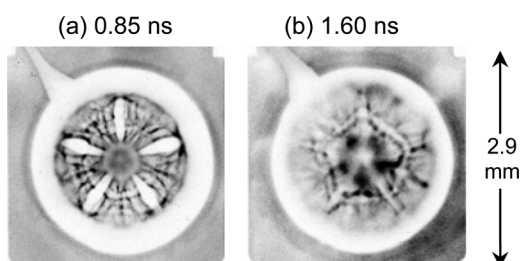


FIG. 16. Radiographs of CH-shell capsules in laser-driven Au hohlraums at OMEGA, recorded along the hohlraum axis with 15-MeV protons at 0.85 ns (a) and 1.6 ns (b) after the onset of a 1-ns laser drive. The light-colored outer ring is the hohlraum wall, and the 5-fold pattern between wall and capsule is due to electric fields generated by laser-hohlraum interactions (see Ref. 33 for more information about these experiments).

wall of the laser-driven radiation cavity (hohlraum) there is *E*-field structure with a very strict symmetry that is directly related to the distribution of laser beams on the inner wall of the hohlraum.³³ If filamentation exists, it is completely dominated in the indirect-drive images by these electric fields.

VIII. DISCUSSION

The coronal fields that allow us to image the filaments appear during the laser drive, grow quickly and saturate, connecting out with the corona even long after the drive is off. Because the filamentation occurs during laser drive, it could have significant impact on the efficiency of the drive itself and also possibly on the formation of hydrodynamic instabilities during capsule implosion. Speculation on the details of plasma structure in and near the filaments is beyond the scope of this paper, but since the filaments appear to fill most of the corona while the drive is on they are likely to result in refraction of laser light² and thereby affect the overall efficiency of conversion of the laser light to thermal energy for ablative drive (as discussed in Ref. 2). In addition, by modifying the spatial distribution of laser light approaching the critical surface, they could make the spatial distribution of heat deposition nonuniform and thereby potentially seed Rayleigh-Taylor instabilities at the ablation surface of normal direct-drive ICF capsules.

It has not been determined for certain whether the filaments extend inward to the ablation surface, which would be predicted if the filaments are generated by the electrothermal instability,¹⁰ but if they do then their fields could inhibit electron thermal transport from the critical surface to the ablation surface.² In addition, the growth of filaments at or near the ablation surface would presumably result in nonuniformities in plasma conditions on the ablation surface and potentially seed Rayleigh-Taylor instabilities for normal direct-drive ICF capsules.²

No definitive demonstration has been given about the exact physical mechanism behind the appearance of filamentation. However, we have learned that the formation of filaments is probably not caused by RT instabilities related to inward shell acceleration (since filaments occurred even with solid subject targets that have little or no radial acceleration) or the TPD instability (since filaments occurred at laser intensities of $\sim 1 \times 10^{14}$ W/cm², well below the instability threshold). No reason has been seen so far to rule out the electrothermal instability,¹⁰ though theoretical predictions of that instability have not been compared to the data.

There is intriguing partial evidence suggesting that we may have observed quasi-spherical electric fields in the corona that could be connected with a previously noted tendency for spectra of radially accelerated ablator protons to contain a series of discrete energy peaks. This focuses our attention on the large-scale movements of charged particles that occur during an implosion, since it is known that protons numbering $\sim 10^{15}$ are accelerated away from the target ablator during 60-beam OMEGA implosions (Fig. 15). If the filament fields result from currents, then the resultant influx of charge that would accumulate on the capsule (as described in

Sec. IV C) is $\sim 2 \times 10^{15}$ protons and would approximately balance the outgoing charge.

Finally, we note that filament-related fields (either E or B) could explain long-wavelength fluence variations seen previously in charged-fusion-product self emission from directly driven implosions.¹³ $D^3\text{He}$ protons generated in imploded fuel capsules were detected on a piece of CR-39 and found to have a nonuniform spatial distribution but no variation in energy. If the coronal filaments were surrounded by either E or B fields, those fields could have deflected the self-emitted protons as they passed from the capsule to the detector and affected their spatial distributions without changing their energies. This raises the question of whether the exploding-pusher backlighters used for radiographs shown in this paper might themselves have had filament-related fields causing nonuniformities in fluence. No backlit radiograph has yet been made of a subject exactly equivalent to a backlighter, but Appendix B discusses a related radiograph and evidence that backlighter nonuniformity does not play a significant role in the images shown here.

IX. FUTURE WORK

A new and large group of radiographs has provided a wealth of new information about coronal filamentation and fields in ICF, providing an introduction to the topic of self-generated fields outside direct-drive implosions. While the conclusions reached here are mostly observational, they provide some guidelines for future computational, theoretical, and experimental work.

In the area of computational work, analytic calculations and Monte Carlo simulations are being pursued in an effort to reach a more definitive conclusion about the nature of the filament fields. In theoretical work, we hope the present data will motivate comparisons of the observations to predictions for various mechanisms (e.g., the electrothermal instability).

Useful experimental investigations of filamentation will consider its sensitivity to a wider range of laser drive intensities. On the low-intensity end, filamentation was seen here at $\sim 1 \times 10^{14}$ W/cm², but another ICF-related experiment¹⁷ at an intensity an order of magnitude lower (1×10^{13} W/cm²) reported none. Is there an intensity threshold? On the high-intensity end, we studied filamentation with drive intensity up to $\sim 6 \times 10^{14}$ W/cm², which is close to the upper limit achievable with 40 OMEGA beams. Targets driven with 60 OMEGA beams cannot be imaged with the method used here, since ~ 20 beams are required to drive the backlighter. But it is possible to drive the target with 60 beams and use a proton backlighter in the form of a foil driven by a short-pulse OMEGA-EP beam. This has been done already, and results will be reported soon. (Similar filamentation is seen, and while the images have somewhat better spatial and temporal resolution they show similar numbers of filaments.) The next step would be imaging direct-drive implosions on the National Ignition Facility,³⁴ where far higher intensities relevant to ignition would be available. Apart from higher intensity, it would be important to try to find a way to actually see whether filaments penetrate into the region between the ablation surface and the critical surface.

Similarly, the data here on spherical charge shells and their possible relationship with ablator proton spectra suffers from the lack of sufficient data for seeing how it evolves and what happens at the time when filamentation dominates image structure. It would be interesting to see whether this phenomenon has a well-defined threshold, since there was no sign of it below intensities of 6×10^{14} W/cm². And does it get stronger at higher intensities? Furthermore, the current lack of any ablator-proton data acquired simultaneously with radiographs needs to be remedied. And the transition from spherical charge shells to filaments should be studied with more time samples. Is this transition a rearrangement of a distribution of net charge?

Some of this work is now being planned and will be aided by supplementary imaging experiments now being executed using implosions with up to 9×10^{14} W/cm² illumination on the OMEGA laser and radiography utilizing protons generated by the interactions of an OMEGA-EP laser beam with foils.²⁸

ACKNOWLEDGMENTS

This work was supported in part by the Laboratory for Laser Energetics (LLE) National Laser User's Facility (DE-FG03-03SF22691) and the Fusion Science Center at the University of Rochester (412761-G). We thank General Atomics for the fabrication of targets; the operations staff and Michelle Burke at LLE for their help with the experiments; and Jocelyn Schaeffer at MIT for data processing. In addition, an anonymous referee provided very useful suggestions.

APPENDIX A: COMPARISON OF TWO TYPES OF IMAGING SYSTEMS

In a joint experiment involving OMEGA shot 55188 and OMEGA-EP shot 5707, two simultaneous proton-radiography images were recorded as 10 OMEGA beams struck a 865- μm -diameter solid CH sphere. One image was formed with the same imaging system described in Sec. II, with spatial resolution ~ 45 μm . The other utilized a backlighter formed by a 10- μm -diameter, 872-J, 10-ps-long beam from OMEGA EP (Ref. 27) striking an Au foil. The 10 OMEGA drive beams were incident on one side of the target, resulting in a surface intensity of $\sim 9 \times 10^{14}$ W/cm², and the results are shown in Fig. 17. Both systems show image striations similar to those seen on symmetrically driven targets described above, as well as some interesting features coming off the opposite side of the spherical target (that have not yet been analyzed or interpreted).

The image comparison is not quite fair, since the exploding-pusher backlighter in this case had a yield much lower than normal, leading to very bad image statistics and low contrast. But the sizes of the image striations are comparable in both images. Therefore, the images obtained with the exploding-pusher backlighters do not lose essential structural information about the striations in spite of the weaker spatial and temporal resolution. More information about other planned work with the EP-based system, including preliminary images of implosions, can be found in Ref. 28.

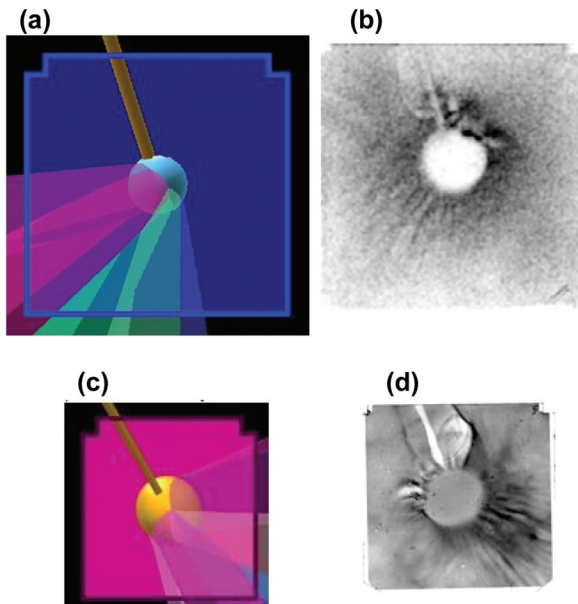


FIG. 17. (Color) Two different images of a CH sphere driven by 10 OMEGA laser beams. Part (a) shows a cartoon of the field of view of an exploding-pusher imaging system as described in Sec. II, and part (b) shows an image recorded with 15-MeV protons about 1 ns after the beginning of laser drive. Part (c) shows the nearly simultaneous field of view of the OMEGA-EP-based imaging system, and part (d) shows the corresponding image recorded with a wider spectrum of protons with an average energy of ~ 15 MeV.

APPENDIX B: RADIOGRAPH OF AN EXPLODING-PUSHER TARGET

Figure 18 shows an image of an exploding-pusher type of shot, involving a capsule with a thin glass shell. This is of specific interest here in connection with the question of whether there are any fields around the backlighter implosions discussed in Sec. II. Fields connected with filaments could generate fluence nonuniformities for the backlighter-generated protons used to make radiographs of other implosions. The capsule whose image is shown in Fig. 18 is not

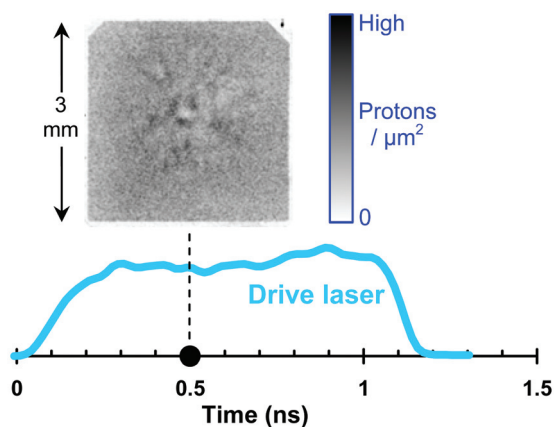


FIG. 18. (Color) 15-MeV-proton radiograph of an 840- μm -diameter capsule with 2- μm -thick glass shell and 15-atm H_2 fill. The capsule was driven with 40 laser beams, with a peak intensity of $\sim 6 \times 10^{14}$ W/cm 2 . The sample time of 0.5 ns is close to what would be bang time if the capsule were filled with D^3He . This was OMEGA shot 51251.

exactly comparable to the backlighter capsules, since it has a diameter twice as large and it is driven with 40 laser beams instead of 20 (among other things, this makes the drive intensity half as large). Nevertheless, this is the only image recorded so far that is relevant to the backlighter itself, and it does show weak filamentation at 0.5 ns, which is close to what bang time would be if the capsule were filled with D^3He and which is slightly later than the bang time (measured by the proton temporal diagnostic²⁴) that has typically been recorded for the backlighters themselves. The weak filamentation does indicate that backlighter-proton fluences could be slightly nonuniform, but the radiographs shown in this paper show very little indication that this is so (see the leftmost images in Figs. 2 and 4).

APPENDIX C: SOME FUTURE EXPERIMENTAL PROJECTS IN RADIOGRAPHY OF DIRECT-DRIVE ICF IMPLOSIONS

1. Radiograph an exploding-pusher backlighter at different times to see if it has significant surrounding fields at bang time.
2. Radiograph imploding, CH-shell capsules at more times to resolve development of charge shells, transition to filamentation, and see how long filamentation survives.
3. Study a wider range of drive intensities to see if charge shells and/or filamentation have a lower threshold of illumination intensity and/or energy and to see what happens at higher illumination intensities than covered here.
4. Collect ablator-ion spectra while recording radiographs that show the types of charge shells seen in Fig. 3.
5. Find a way to determine whether filaments penetrate into the region between the ablation surface and the critical surface.
6. Use backlighters driven by short-pulse, petawatt lasers such as OMEGA EP to see whether the improved spatial and temporal resolution achievable in this way reveals any fundamentally different phenomena.
7. Radiograph direct-drive implosions on the NIF, where far higher drive intensities relevant to ignition would be available.

¹S. Atzeni and J. Meyer-ter-Vehn, *The Physics of Inertial Fusion* (Oxford University Press, New York, 2004).

²M. G. Haines, *Can. J. Phys.* **64**, 912 (1986).

³B. Grek, F. Martin, T. W. Johnston, H. Pépin, G. Michel, and F. Rheault, *Phys. Rev. Lett.* **41**, 1811 (1978).

⁴T. Mochizuki, T. Yaabe, K. Mima, K. Yoshikawa, H. Azechi, A. Kikuchi, and C. Yamanaka, *Jpn. J. Appl. Phys.* **19**, L645 (1980).

⁵O. Willi, P. T. Rumsby, and C. Duncan, *Opt. Commun.* **45**, 40 (1981).

⁶O. Willi and P. T. Rumsby, *Opt. Commun.* **37**, 45 (1981).

⁷G. Thiell and B. Meyer, *Laser Part. Beams* **3**, 51 (1985).

⁸M. Borghesi, D. H. Campbell, A. Schiavi, M. G. Haines, O. Willi, A. J. MacKinnon, P. Patael, L. A. Gizzi, M. Galimberti, R. J. Clarke, F. Pegoraro, H. Ruhl, and S. Bulanov, *Phys. Plasmas* **9**, 2214 (2002).

⁹A. J. Mackinnon, P. K. Patel, R. P. Town, M. J. Edwards, T. Phillips, S. C. Lerner, D. W. Price, D. Hicks, M. H. Key, S. Hatchett, S. C. Wilks, M. Borghesi, L. Romagnani, S. Kar, T. Toncian, G. Pretzler, O. Willi, M. Koenig, E. Martinolli, S. Lepape, A. Benuzzi-Mounaix, P. Audebert, J. C. Gauthier, J. King, R. Snively, R. R. Freeman, and T. Boehlly, *Rev. Sci. Instrum.* **75**, 3531 (2004).

¹⁰M. G. Haines, *Phys. Rev. Lett.* **47**, 917 (1981).

- ¹¹C. K. Li, G. Hicks, F. H. Seguin, J. A. Frenje, R. D. Petrasso, J. A. Soures, P. B. Radha, V. Yu. Glebov, C. Stoeckl, D. R. Harding, J. P. Knauer, R. Kremens, F. J. Marshall, D. D. Meyerhofer, S. Skupsky, S. Roberts, C. Sorce, T. C. Sangster, T. W. Phillips, M. D. Cable, and R. J. Leeper, *Phys. Plasmas* **7**, 2578 (2000).
- ¹²D. G. Hicks, C. K. Li, F. H. Seguin, J. A. Frenje, R. D. Petrasso, J. A. Soures, V. Yu. Glebov, D. D. Meyerhofer, S. Roberts, C. Sorce, C. Stoeckl, T. C. Sangster, and T. W. Phillips, *Phys. Plasmas* **7**, 5106 (2000).
- ¹³F. H. Seguin, C. K. Li, J. A. Frenje, S. Kurebayashi, R. D. Petrasso, F. J. Marshall, D. D. Meyerhofer, J. M. Soures, T. C. Sangster, C. Stoeckl, J. A. Delettrez, P. B. Radha, V. A. Smalyuk, and S. Roberts, *Phys. Plasmas* **9**, 3558 (2002).
- ¹⁴C. K. Li, F. H. Seguin, J. A. Frenje, J. R. Rygg, R. D. Petrasso, R. P. J. Town, P. A. Amendt, S. P. Hatchett, O. L. Landen, A. J. Mackinnon, and P. K. Patel, *Phys. Rev. Lett.* **97**, 135003 (2006).
- ¹⁵C. K. Li, F. H. Seguin, J. R. Rygg, J. A. Frenje, M. Manuel, R. D. Petrasso, R. Betti, J. Delettrez, J. P. Knauer, F. Marshall, D. D. Meyerhofer, D. Shvarts, V. A. Smalyuk, C. Stoeckl, O. L. Landen, R. P. J. Town, C. A. Back, and J. D. Kilkenny, *Phys. Rev. Lett.* **100**, 225001 (2008).
- ¹⁶J. R. Rygg, F. H. Séguin, C. K. Li, J. A. Frenje, M. J.-E. Manuel, R. D. Petrasso, R. Betti, J. A. Delettrez, O. V. Gotchev, J. P. Knauer, D. D. Meyerhofer, F. J. Marshall, C. Stoeckl, and W. Theobald, *Science* **319**, 1223 (2008).
- ¹⁷A. J. Mackinnon, P. K. Patel, M. Borghesi, R. C. Clarke, R. R. Freeman, H. Habara, S. P. Hatchett, D. Hey, D. G. Hicks, S. Kar, M. H. Key, J. A. King, K. Lancaster, D. Neely, A. Nikkro, P. A. Norreys, M. M. Notley, T. W. Phillips, L. Romagnani, R. A. Snavely, R. B. Stephens, and R. P. J. Town, *Phys. Rev. Lett.* **97**, 045001 (2006).
- ¹⁸N. A. Ebrahim, H. A. Baldis, C. Joshi, and R. Benesch, *Phys. Rev. Lett.* **45**, 1179 (1980).
- ¹⁹D. G. Hicks, C. K. Li, F. H. Seguin, J. D. Schnittman, A. K. Ram, J. A. Frenje, R. D. Petrasso, J. M. Soures, D. D. Meyerhofer, S. Roberts, C. Sorce, C. Stoeckl, T. C. Sangster and T. W. Phillips, *Phys. Plasmas* **8**, 606 (2001).
- ²⁰D. G. Hicks, Ph.D. thesis, Massachusetts Institute of Technology, 1999.
- ²¹T. R. Boehly, D. L. Brown, R. S. Craxton, R. L. Keck, J. P. Knauer, J. H. Kelly, T. J. Kessler, S. A. Kumpan, S. J. Loucks, S. A. Letzring, F. J. Marshall, R. L. McCrory, S. F. B. Morse, W. Seka, J. M. Soures, and C. P. Verdon, *Opt. Commun.* **133**, 495 (1997).
- ²²C. Stoeckl, R. E. Bahr, B. yaakobi, W. Seka, S. P. Regan, R. S. Craxton, J. A. Delettrez, R. W. Short, J. Myatt, A. V. Maximov, and H. Baldis, *Phys. Rev. Lett.* **90**, 235002 (2003).
- ²³F. H. Seguin, J. A. Frenje, C. K. Li, D. G. Hicks, S. Kurebayashi, J. R. Rygg, B.-E. Schwartz, R. D. Petrasso, S. Roberts, J. M. Soures, D. D. Meyerhofer, T. C. Sangster, J. P. Knauer, C. Sorce, V. Yu. Glebov, C. Stoeckl, T. W. Phillips, R. J. Leeper, K. Fletcher, and S. Padalino, *Rev. Sci. Instrum.* **74**, 975 (2003).
- ²⁴J. A. Frenje, C. K. Li, F. H. Séguin, J. Deciantis, J. R. Rygg, B.E. Schwartz, S. Kurebayashi, R. D. Petrasso, J. Delettrez, V. Yu. Glebov, F. J. Marshall, D. D. Meyerhofer, T. C. Sangster, C. Stoeckl, and J. M. Soures, *Phys. Plasmas* **11**, 2798 (2004).
- ²⁵F. H. Séguin, J. L. DeCiantis, J. A. Frenje, S. Kurebayashi, C. K. Li, J. R. Rygg, C. Chen, V. Berube, B. E. Schwartz, R. D. Petrasso, V. A. Smalyuk, F. J. Marshall, J. P. Knauer, J. A. Delettrez, P. W. McKenty, D. D. Meyerhofer, S. Roberts, T. C. Sangster, K. Mikaelian, and H. S. Park, *Rev. Sci. Instrum.* **75**, 3520 (2004).
- ²⁶C. K. Li, F. H. Séguin, J. A. Frenje, J. R. Rygg, R. D. Petrasso, R. P. J. Town, P. A. Amendt, S. P. Hatchett, O. L. Landen, A. J. Mackinnon, P. K. Patel, V. A. Smalyuk, J. P. Knauer, T. C. Sangster, and C. Stoeckl, *Rev. Sci. Instrum.* **77**, 10E725 (2006).
- ²⁷L. Waxer, D. Maywar, J. Kelly, T. Kessler, B. Kruschwitz, S. Loucks, R. McCrory, D. Meyerhofer, S. Morse, C. Stoeckl, and J. Zuegel, *Opt. Photonics News* **16**, 30 (2005).
- ²⁸A. B. Zylstra, C. K. Li, H. G. Rinderknecht, F. H. Seguin, R. D. Petrasso, C. Stoeckl, D. D. Meyerhofer, P. Nilson, C. Sangster, S. Le Pape, A. Mackinnon, and P. Patel, "Using high intensity laser-generated energetic protons to radiograph directly driven implosions," *Rev. Sci. Instrum.* (to be published).
- ²⁹J. Delettrez, R. Epstein, M. C. Richardson, P. A. Jaanimagi, and B. L. Henke, *Phys. Rev. A* **36**, 3926 (1987).
- ³⁰P. Mora, *Phys. Rev. Lett.* **90**, 185002 (2003).
- ³¹Nelson Hoffman, private communication (2007).
- ³²C. K. Li, F. H. Seguin, J. A. Frenje, R. D. Petrasso, P. A. Amendt, R. P. J. Town, O. L. Landen, J. R. Rygg, R. Betti, J. P. Knauer, D. D. Meyerhofer, J. M. Soures, C. A. Back, J. D. Kilkenny, and A. Nikroo, *Phys. Rev. Lett.* **102**, 185004 (2009).
- ³³C. K. Li, F. H. Séguin, J. A. Frenje, M. Rosenberg, R. D. Petrasso, P. A. Amendt, J. A. Koch, O. L. Landen, H. S. Park, H. F. Robey, R. P. J. Town, A. Casner, F. Philippe, R. Betti, J. P. Knauer, D. D. Meyerhofer, C. A. Back, J. D. Kilkenny, and A. Nikroo, *Science* **327**, 1231 (2010).
- ³⁴G. H. Miller, E. I. Moses, and C. R. Wuest, *Nucl. Fusion* **44**, S228 (2004).